# Air-Data Estimation for Air-Breathing Hypersonic Vehicles

Bryan Heejin Kang

**Abstract** : An air-data estimator for generic air-breathing hypersonic vehicles (AHSVs) is developed and demonstrated with an example vehicle configuration. The AHSV air-data estimation strategy emphasized improvement of the angle of attack estimate accuracy to a degree necessitated by the stringent operational requirements of the air-breathing propulsion. The resulting estimation problem involves highly nonlinear diffusion process (propagation); consequently, significant distortion of a posteriori conditional density is suspected. A simulation based statistical analysis tool is developed to characterize the nonlinear diffusion process. The statistical analysis results indicate that the diffusion process preserves the symmetry and unimodality of initial probability density shape of state variables, and provide the basis for applicability of an Extended Kalman Filter (EKF). An EKF is designed for the AHSV air-data system and the air data estimation capabilities are demonstrated.

**Keywords** : estimation, control, hypersonic propulsion

## I. Introduction

Enthusiasm for hypersonic flight research has been renewed by the promise of a fully reusable, horizontal take off, single stage to orbit flight vehicle with air-breathing engines. Projected air-breathing hypersonic vehicles (AHSVs), such as was envisioned with the X-30 or National Aero-Space Plane (NASP) program, would potentially be very efficient [1]. A unique feature of this class of vehicles is the usage of air-breathing engines as the main propulsion system during most of the ascent trajectory. Since typical launch vehicles may allocate up to 90% of the vehicle weight to fuel and oxidizer, using atmospheric oxygen significantly reduces vehicle weight when compared to the rocket propulsion system with similar payload capability.

Operational requirements of an air-breathing hypersonic vehicle differ in many ways from conventional spacecraft and aircraft, mainly due to its unique propulsion system. Design of an air-breathing hypersonic vehicle will emphasize air-breathing engine performance and stability. As shown in Fig. 1, the vehicle lower surface would act as inlet and nozzle while providing lift. Consequently, AHSVs will have propulsion, aerodynamics, and flight dynamics that are highly integrated and interactive [1]-[3]. The flight control, guidance, engine control and vehicle cooling are heavily coupled to provide the proper combustion conditions.

The performance and stability of the air-breathing engines can be characterized only if the nominal and perturbations of the vehicle attitude in the wind frame are specified. Past investigations of the sensitivity of

Manuscript received : June. 11, 1998., Accepted : Dec. 19, 1998.
*Bryan Heejin Kang* : Senior Research Engineer, S&TD Avionics, TRW Los Angeles, CA, USA.
※ This research was funded by the Charles Stark Draper Laboratory, Cambridge, MA, USA.

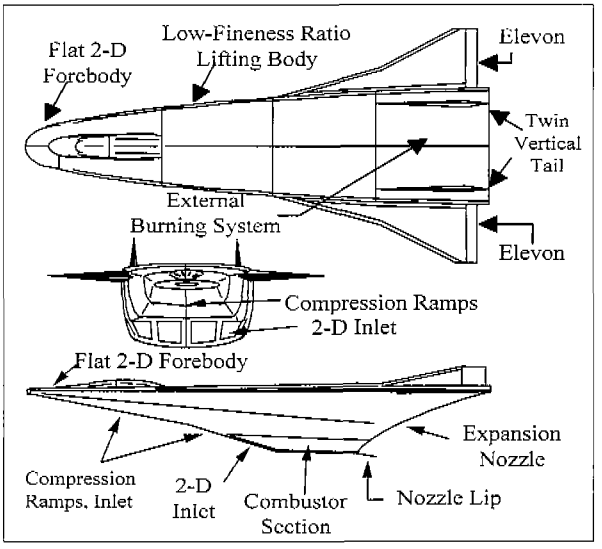


Fig. 1. AHSV configurations.

ramjet and Scramjet performance with respect to air data parameters indicated that the operation of the air-breathing engines outside the design envelope severely degrades the propulsion efficiency and could lead to combustion instability [4][5]. Consequently, the air-data parameters must be accurately estimated on board, in real time, to ensure proper operation of the AHSV propulsion system.

## II. Air data estimation requirements

Accuracy requirements for AHSV air-data state are derived from the unique propulsion and control requirements [4][6][7]. The AHSV trajectory optimization and performance sensitivity results are used to define the requirements. A summary of the requirements is in Table 1 below [4][7]. The most stringent requirements are imposed on the flow direction parameters such as angle of attack and side slip angle. Additional 5% fuel consumption will occur if angle of

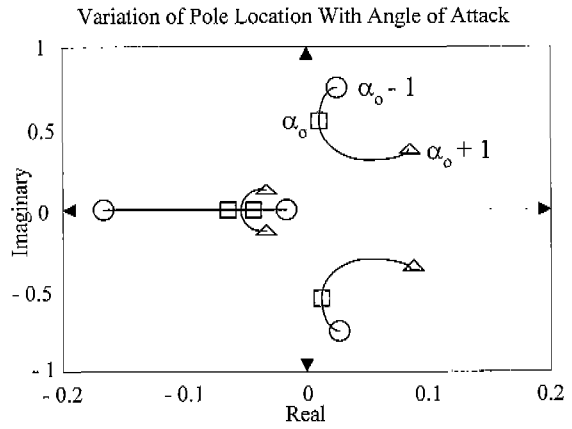


Fig. 2. Sensitivity of the lincarized system to attitude variations.

attack is changed by one degree from the design value [6].

The angle of attack requirement for the AHSV flight control system is extremely stringent. The AHSVs exhibit highly nonlinear dynamics with respect to the angle of attack variations. In order to demonstrate the sensitivity, the AHSV nonlinear dynamics have been linearized numerically at a number of angles of attack within a few degrees of the design flight condition. The results, shown in Fig. 2, dramatically illustrate the sensitivity of the linearized system to changes in angle of attack. The curves shown represent the movement of the phugoid and short period poles as a function of angle of attack. Note that only a two degree changes in angle of attack significantly alters the dynamic properties of the longitudinal modes.

In order to stabilize and regulate the AHSV propulsion and flight control system, 0.1° angle of attack and side slip accuracy requirements are imposed. However, 0.1° accuracy requirements in angle of attack and side slip measurements are difficult to meet with the currently available air-data sensors. An engine sensitivity analysis6 notes that the free stream conditions such as temperature, density and pressure will also dictate the air-breathing engine's performance.

Table 1. Air-Data requirements.

| States | Required Accuracy | Range |
|---|---|---|
| $\alpha$ anlgle of attack | 0.1° | -5° to +30° |
| $\beta$ side slip | 0.1° | ± 5° |
| $Q$ dynamic pressure | 5% | up to 2000 psf |
| $\rho_\infty$ free stream density | 0.5% | up to 0.0025 slug/ft$^3$ |
| $T_\infty$ free stream temp. | 0.5% | 360°R to 560°R |
| $V_a$ air relative velocity | 0.5% | 0 to 28,000 fps |

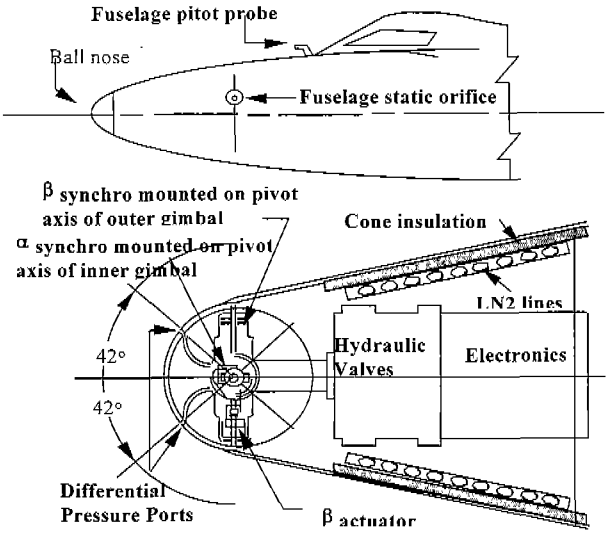


Fig. 3. Schematic drawing of the X-15 ball nose sensor.

## III. Historic overview of hypersonic air data instrumentation

Only a few hypersonic flight vehicles, from which to draw hypersonic instrumentation technology, currently exist. Among these, the X-15 and the Space Shuttle Orbiter are the most significant..

X-15 Ball Nose Sensor : The X-15 was a rocket-propelled hypersonic research aircraft. It had typical missions of rocket powered boost from 40kft to about 200kft with a ballistic coast to a maximum height of 350kft while traveling at flight Mach numbers up to 7. Reentry occurred at a high angle of attack to dissipate energy while maintaining the skin temperature below the 1200° F. The hypersonic flight segment typically lasted 10 to 15 minutes [9]. As shown in Fig. 3, the sphere was housed in the end of the conic nose..

It was rotated by a hydraulic actuator to face the stream-wise direction by nulling the differential pressure between vertical and lateral pressure sensor pairs. The alignment angles of the sphere with respect to the aircraft reference axis indicated the angles of attack and of side slip. The rear portion of the sphere contained the mechanical and electrical components. These components, along with the sphere, were cooled by vaporized liquid nitrogen. Thus, the X-15 structure and associated components behind stagnation points were capable of withstanding temperature of up to approximately 1200° F (922 K).

Space Shuttle : The reentry phase of the shuttle flight [10] spans the Mach numbers from 27 to touch down, the angle of attack from -5° to 45°, and the peak stagnation temperature up to about 2000° F to 2300° F (1366 K to 1532 K). The Shuttle Entry Air Data System (SEADS), designed for hypersonic flight experimentation, is currently mounted on the Shuttle Columbia since the STS 61-C mission and is used to

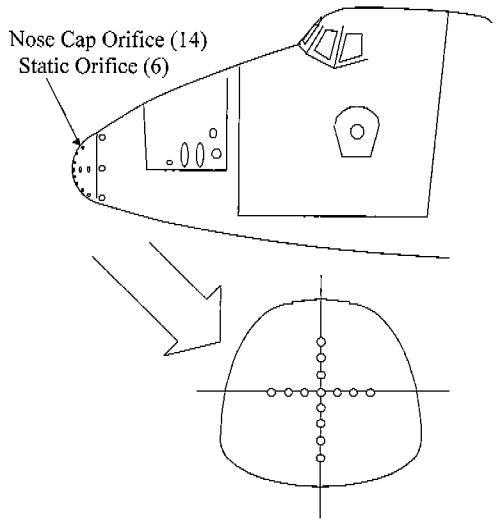


Fig. 4. SEADS orifice configuration.

collect atmospheric research data during entry operations [11]. As shown in Fig. 4, the SEADS employs a cruciform array of 14 flush mounted pressure transducers on the nose cap as well as 6 static orifices located aft of the nose cap.

The nose cap heating rates can reach 50 W/cm$^2$. The nose of the Shuttle Orbiter functions as both a Pitot-static probe and a flow direction sensor by implementing numerical pressure sensor data processing techniques [1][12]. A computational technique, which includes calibration parameters derived from wind tunnel data, is used to extract air-data parameters from the pressure field measurements without a rotating ball nose. A rotating ball like the one used on the X-15 would have an operational Mach limit too low for the Shuttle.

### Ⅳ. Applicable ahsv air data aensor technology

From the list of existing or conceptual hypersonic sensors, several workable concepts are selected so that, in the aggregate, they constitute a satisfactory sensor package. Both pressure and optic based air-data sensors were considered for the AHSV applications. Among the pressure based sensor technologies, the flush mounted pressure port sensors like the Shuttle Entry Air Data System (SEADS) are considered. The Rayleigh scattering and Laser induced fluorescence (LIF) techniques are selected for the AHSV sensor set as the most promising optical sensor technology.

Pressure based SEADS-like sensor system : Multiple pressure sensors are flush mounted on the nose section of the vehicle. The surface pressure distribution is measured by the array of flush mounted sensors. A mathematical description of the forebody pressure distribution is used to obtain the air data state parameters..

On the basis of the modified Newtonian flow model, the pressure at the i-th orifice can be written as :

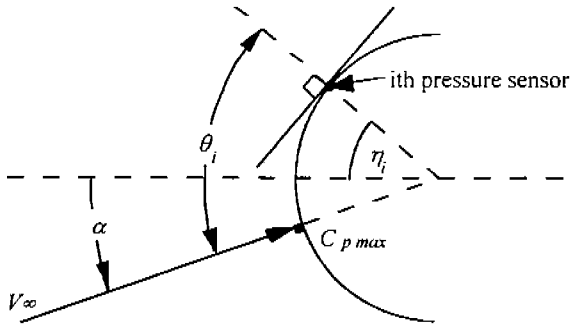


Fig. 5. Modified newtonian approximation of round nose.

$$P_i = (P_t - P_\infty)\cos^2\theta_i + P_\infty \quad \text{for} \quad M_\infty \gg 1 \tag{1}$$

where $\theta_i$ is the flow incident angle at the i-th orifice (90° incidence, the flow angle to the normal to the surface). The $\theta_i$ can be written as:

$$\begin{aligned}\cos\theta_i = {} & \cos\alpha\cos\beta\cos\eta_i + \sin\beta\sin\eta_i\cos\zeta_i \\ & + \sin\alpha\cos\beta\sin\eta_i\sin\zeta_i\end{aligned} \tag{2}$$

where $\eta_i$ is the cone angle and $\zeta_i$ is the clock angle. If only the longitudinal motion is considered, as shown in Fig. 5, the equations (1) and (2) simplify to:

$$P_i = P_t[(1 - R(M_\infty))\cos^2(\alpha + \eta_i) + R(M_\infty)]$$
$$\text{for} \quad M_\infty \gg 1 \tag{3}$$

where the Rayleigh Pitot formula is:

$$R \equiv \frac{P_\infty}{P_t} = \left[\frac{2}{(\gamma+1)M_\infty^2}\right]^{\frac{\gamma}{\gamma-1}}\left[\frac{2\gamma M_\infty^2 - (\gamma-1)}{\gamma+1}\right]^{\frac{1}{\gamma-1}}$$
$$\text{for} \quad M_\infty > 1 \tag{4}$$

where $P_t$ is total pressure.

Rayleigh scattering sensor : Rayleigh scattering is an elastic scattering process where the frequency of the scattered light is well removed from a resonance in the atom. The scattered intensity is proportional to the density of scattering molecules. The broadening of the scattered light spectrum is dependent on the temperature of scattering molecules and the Doppler shift is dependent on the mean molecular velocity.

A Rayleigh scattering sensor may operate in a wide altitude range, up to well over 200kft. The upper altitude bound is determined by the loss of return signal due to low scattering particle density. The lower bound is set by excessive Mie scattering effects at low altitude due to high concentration of entrained particles. Functional block diagram of the Rayleigh Scattering sensor is shown in Fig. 6.

The Doppler shift in Rayleigh scattered light can be measured by spectroscopic equipment, such as the scanning Fabry-Perot etalon. The Doppler shift fre-

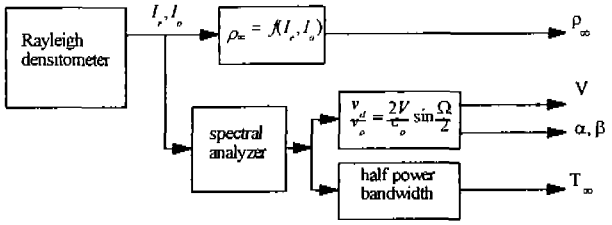


Fig. 6. Block diagram of rayleigh scattering sensor.

quency and the flow velocity are related by the expression below:

$$\frac{v_d}{v} = \frac{2V}{c} \sin\frac{\Omega_o}{2} \tag{5}$$

where $v_d$ is the Doppler shift frequency, v is the laser frequency, c is the speed of light, V is the flow velocity. Three orthogonal sensors are needed to resolve all velocity components.

The major measurement error is in the process of resolving the median frequency from the broadened spectrum. Another measurement error arises from the spatial resolution and alignment error at the sensing section of the laser beam. The accuracy of this technique is estimated to be about ±2.5%[14] with the spatial resolution of ±0.75°. If a specially designed molecular filter is used to resolve the 50% transmission point, the Rayleigh scattering device can measure the velocity of a sample to about 0.3% at 30km altitude [15].

The performance degrades as altitude increases, because the sensor performance is limited by photoelectron shot noise from the detected signal that increases with altitude. At 60km, the measurement uncertainty is expected to increase to 2%; and will further increase to 19% at 90km altitude.

The sensor noise can be modeled as shot noise with standard deviation proportional to the square root of the number of detected Rayleigh photons as shown in equation (6).

$$\text{Noise Intensity} = \left[\frac{I_r h\nu}{\wedge t N_p}\right]^{1/2} \tag{6}$$

The measured velocities of sampled air are coordinate transformed to body axes to represent flow parameters as shown in Fig.* 7. The resulting measurement equation is:

$$u_i(t) = V(t)\cos(\theta_i + \alpha(t)) + n_i(I_r, altitude, t) \tag{7}$$

where $u_i$ is the velocity measurement along the sensing axis, V is the true air velocity and the $n_i$ is the associated velocity measurement noise.

Laser Induced fluorescence sensor : The laser induced fluorescence technique uses the properties of the electromagnetic wave induced resonance of the

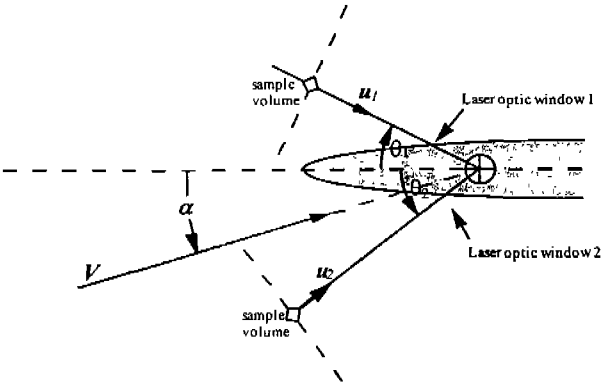


Fig. 7. Sensing coordinate for rayleigh scattering sensors.

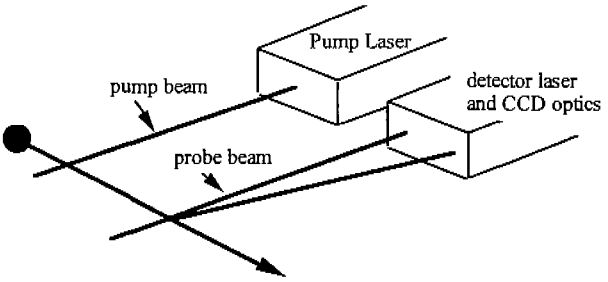


Fig. 8. LIF laser and optical system configuration.

scattering particles [13]. When the laser frequency is tuned to the resonant frequency, which is a unique signature of the tracing molecules, the particle fluoresces at the resonant frequency and generates stimulated emission. A fluorescence tracking velocimetry uses a laser beam to coherently pump(tag) a small volume of gas upstream to meta-stable level, then another laser which is located downstream elevates the energy of the pre-tagged volume. When the energy level of the molecule reaches a critical point, an electron decays and creates fluorescence. Only the pre-tagged volume will respond to the sensing beam since only the energy level of the pre-tagged molecules will be resonant with the sensing beam frequency. The optical detector is used to sense the presence of the fluorescence. The sensor configuration is demonstrated in Fig. 8.

The velocity is approximated by

$$V \approx \frac{X_{detector} - X_{tag}}{\Delta t} \tag{8}$$

which is the difference between the detector position and tagging position divided by the time of travel. The major error source is the spatial misalignment. Both angular position and magnitude error can result from misalignment of the tagging beam and the detector. The measurement noise would be a combination of spatial uncertainties and the false threshold of the fluorescence detection. The threshold of the detectable

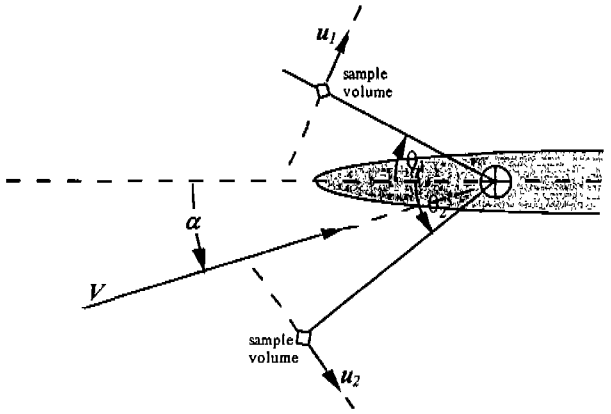


Fig. 9. Sensing coordinate for LIF sensors.

signal strength is dependent on altitude; and can be expressed as:

$$|S_m(h)| = |S(h)| \pm |S(h)| \exp\{6.9(h/h_0 - 2)\} \quad (9)$$

where $S_m$ is the measured detector signal, S is the true signal, and h is the altitude in ft., $h_o$ is a constant with value of 300k ft. The noise is dependent on both the signal and the altitude.

The overall sensor placement and configuration are shown in Fig. 9 below.

The resulting measurement equation is:

$$u_i(t) = V(t)\cos(\theta_i + \alpha(t)) + n_i(S_n, altitude, t) \quad (10)$$

where ui is the velocity measurement, V is the true air velocity and the $n_i$ is the associated velocity measurement noise.

## V. Ahsv dynamics: diffusion process

In order to formulate the estimation problem for AHSV air data parameters, the diffusion equations that govern the time evolution of the air data state conditional densities are formulated from AHSV flight and propulsion dynamics.

For the demonstration of estimation process at Mach 10 to 15 regime, a vehicle model was formulated in an LVLH frame. This model was derived based on the assumption of rigid body motions through the atmosphere of a rotating spherical Earth. Currently, the longitudinal motions are only considered with an equatorial launch to orbit scenario. The AHSV model will be updated when lateral propulsion and aerodynamic data are available. The gravitational acceleration has been modeled with altitude variations. A stationary atmosphere with no wind is assumed.

The forcing and control coefficients are obtained numerically from the AHSV design simulator developed in Charles Stark Draper Lab. The simulator contains hypersonic flow and propulsion models that employed panel methods and chemical reaction properties. For simplicity, the aerodynamic and control

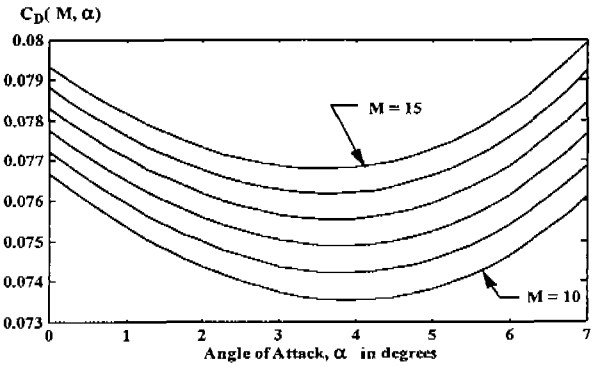


Fig. 10. Plot of drag coefficient.

coefficients are further parameterized by applying polynomial approximations to the tabulated coefficient data. The resulting equations that describe the vehicle motion are[16]:

$$\dot{V} = [\omega_E^2 R - g(R)]\sin(\theta - \alpha) + Q_n[C_{Tv}(M, \alpha, R) - C_D(M, \alpha)] + Q_n[C_{x\delta_e}(M, \alpha, \delta_e) + C_{x\delta_T}(M, \alpha, \delta_T)] + Q_n[C_{x\delta_v}(M, \alpha, \delta_v)[C_{Tv}(M, \alpha, R) + C_{x\delta_T}(M, \alpha, \delta_T)]] \quad (11)$$

$$\dot{\alpha} = \left[\frac{g(R)}{V} - \frac{V}{R} - \frac{\omega_E^2 R}{V}\right]\cos(\theta - \alpha) + q - 2\omega_E + \frac{Q_n}{V}[C_{Tn}(M, \alpha, R) + C_L(M, \alpha) - C_{z\delta_e}(M, \alpha, \delta_e) - C_{z\delta_T}(M, \alpha, \delta_T)] - \frac{Q_n}{V}[C_{z\delta_v}(M, \alpha, \delta_v)[C_{z\delta_T}(M, \alpha, \delta_T) - C_{Tn}(M, \alpha, R)]] \quad (12)$$

$$\dot{q} = \frac{Q_n mc}{I_y}[C_{mp}(M, \alpha, R) + C_{ma}(M, \alpha) + C_{m\delta_e}(M, \alpha, \delta_e) + C_{m\delta_T}(M, \alpha, \delta_T) + C_{m\delta_v}(M, \alpha, \delta_v)[C_{m\delta_T}(M, \alpha, \delta_T) + C_{mp}(M, \alpha, R)]] \quad (13)$$

$$\dot{\theta} = q \quad (14)$$

$$\dot{R} = V\sin(\theta - \alpha) \quad (15)$$

where Normalized Dynamic Pressure $Q_n \equiv \frac{Q(R, V)S}{m}$ and the state $V$ is true air velocity; $\alpha$ is angle of attack; $q$ is pitch rate; $\theta$ is pitch angle; and $R$ is altitude. The parameters, $\omega_E$ is earth rotation rate; $g$ is gravity; $S$ is wing area; $c$ is wing chord length; $m$ is vehicle total mass, and $I_y$ is pitch axis moment of inertia. The control variables are $\delta_e$, $\delta_T$, and $\delta_v$ for elevon, throttle and thrust vectoring respectively.

The aerodynamic and control coefficients are obtained numerically from the simulator and their empirical approximating functions are plotted in Figs 10 to 18 to illustrate the example behavior of the AHSV dynamics. These results are based on a nominal vehicle design optimized for Mach 10 to 15 flight, and the characteristics can change if the AHSV is outside the design envelope.

The approximating functions that describe the throttle and thrust vectoring control coefficients are stated in equation (16) through (21).

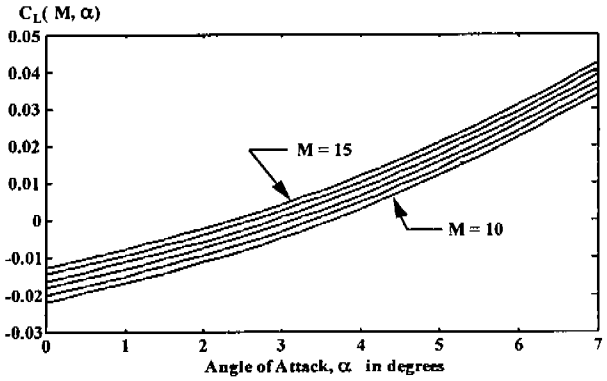


Fig. 11. Plot of lift coefficient.

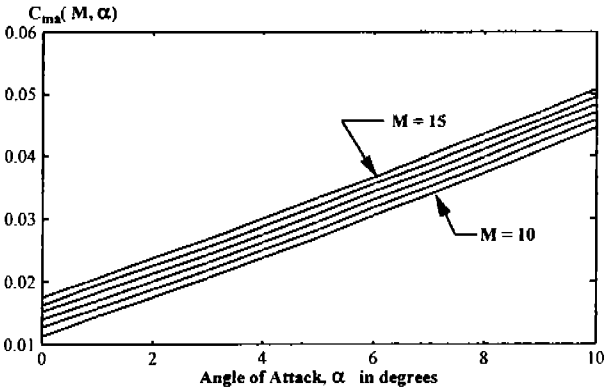


Fig. 12. Plot of moment coefficient.

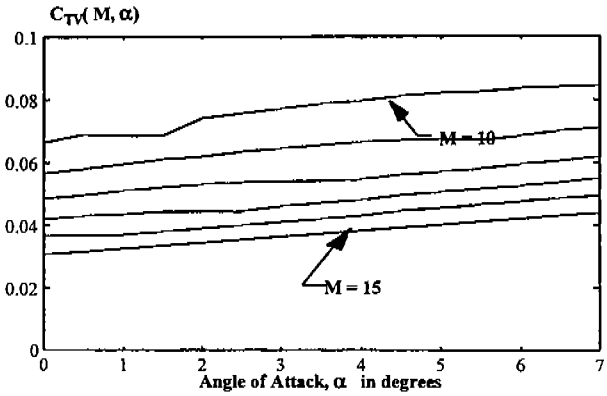


Fig. 13. Thrust coefficient - axial component.

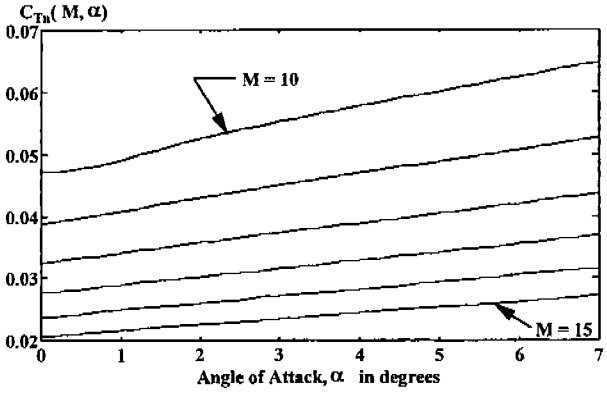


Fig. 14. Thrust coefficient - normal component.

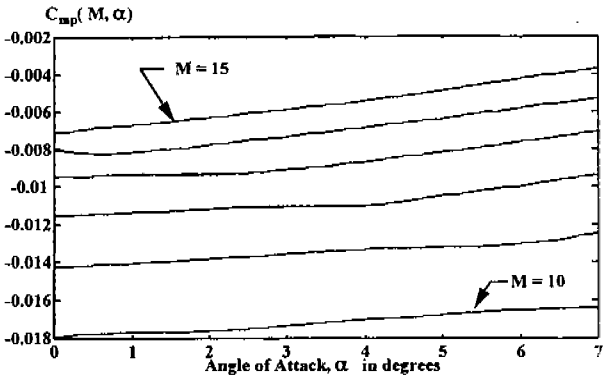


Fig. 15. Propulsion moment coefficient.

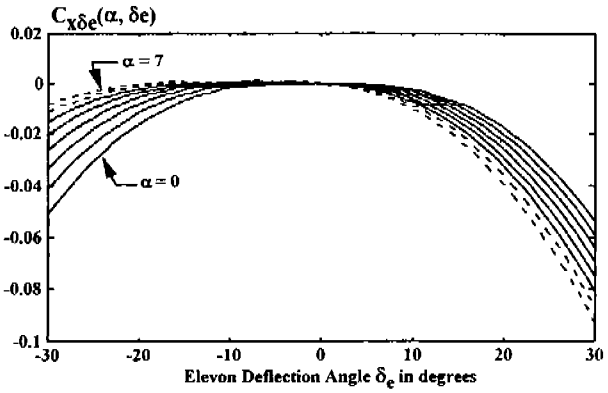


Fig. 16. Elevon control coefficient - X-direction.

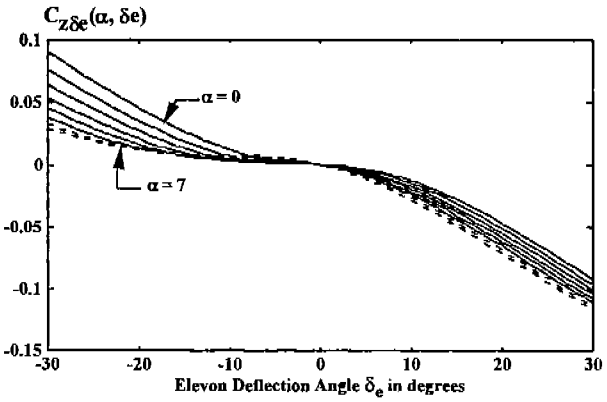


Fig. 17. Elevon control coefficient - Z-direction.

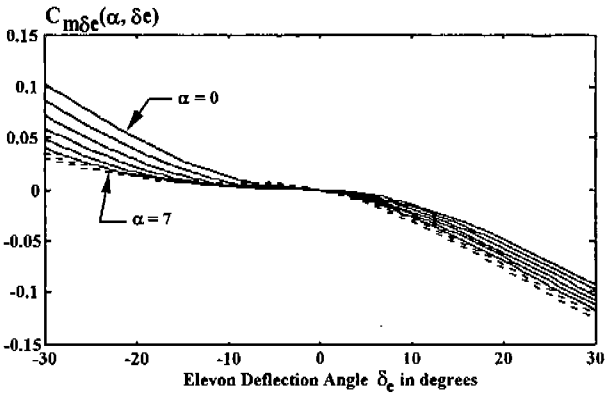


Fig. 18. Elevon control moment coefficient.

Throttle Control Coefficients:

$$C_{x\delta_T} \approx C_{Tv}\,\delta_T \tag{16}$$

$$C_{z\delta_t} \approx C_{Tn}\,\delta_T \tag{17}$$

$$C_{m\delta_T} \approx C_{mp}\,\delta_T \tag{18}$$

Thrust Vectoring Coefficients:

$$C_{x\delta_v} \approx -C_{Tv}\tan(\alpha+\Psi_{T0})\delta_v \tag{19}$$

$$C_{z\delta_v} \approx C_{Tn}\cot(\alpha+\Psi_{T0})\delta_v \tag{20}$$

$$C_{m\delta_t} \approx C_{mp}\cot(\Psi_{T0})\delta_v \tag{21}$$

where $\Psi_{T0}$ are the nominal throttle setting.

Incorporating AHSV Flight Controller Dynamics: The estimation and control problems are coupled since the evolution of the state conditional probability density function (PDF) depends upon control variables. For example, if a full state feedback is considered for generic vehicle equations as shown in equation (22), then the evidence follows when the associated Zakai equation[23] is examined. The time rate of change in the conditional densities depends on state variables, time, control variables, and measurements.

$$\begin{aligned} dx &= f(x,t)dt + f_u(x,u,t)dt + g(x,t)dw \\ u &= K_c(x,t) \\ dz &= h(x,t)dt + dn \end{aligned} \tag{22}$$

$$\begin{aligned} \frac{\partial p^+}{\partial t} = {} & Lp^+(x_t,t)dt + h(x_t,t)R^{\frac{1}{2}}P^+(x_t,t)dy_t \\ & -\frac{1}{2}h(x_t,t)^T R^{-1}h(x_t,t)p^+ \end{aligned} \tag{23}$$

where the Fokker-Planck operator L is

$$L(\cdot) = \sum_i \frac{\partial}{\partial x_i}(f_i(x_i,t)\cdot) + \frac{1}{2}\sum_{j,k}\frac{\partial}{\partial x_j \partial x_k}(g_j(x_t,t)g_k(x_t,t)\cdot) \tag{24}$$

For high Mach number flight, there exists a stable controller design by Chamitoff [8] whose design is based upon Lyapunov stability criterion and an A star search method applied in a manner similar to that used in nonlinear dynamic programming. However, when considering the estimator design, it is undesirable to have the controller in a form of numerical search codes; rather, an analytic form, especially a regulatory feedback controller, is highly attractive.

A simple linearized controller has been implemented for the design of the AHSV air data estimator [16]. For simplicity, the controller is designed based on a linearization about the scheduled state trajectory, and Linear Quadratic Regulator implementation using the linearized model [16]. The constraints are defined by the limitations on the acceleration magnitude due to propulsion, structural dynamics, and human factors. The resulting feedback gains were scheduled to cover the entire Mach 10 to 15 flight.

## VI. Estimation problem formulation

Model based estimation strategy is considered for the air data estimation problem. The AHSV dynamics equations ((11) through (15)) can be summarized as:

$$\begin{aligned} &\dot{x} = f(x,t) + f_u(x,u,t) \\ &\text{with controller} \quad u = K(x,t) \end{aligned} \tag{25}$$

The diffusion process for estimation is defined as the difference between the true state and its prediction. Therefore the equation (25) is rewritten as perturbations about nominal state and control trajectories as shown in equation (26). For nominal trajectory xs and us, the error dynamics can be expanded as:

Let $x_e = x - x_s$ and $u_e = u - u_s$ then

$$\dot{x_e} = \dot{x} - \dot{x_s} = f(x_s + x_e, t) + f_u(x_s + x_e, u_s + u_e, t) \tag{26}$$

During high Mach number flight at high altitudes, the disturbances are predominantly caused by atmospheric density fluctuations. For any given time, the free stream density is spatially distributed over the flight trajectory. As the AHSV fly through that density field, the disturbances can be observed as a Markovian random processes. With the density disturbance model, the diffusion process becomes:

$$\dot{x_e} = \dot{x} - \dot{x_s} = f(x_s + x_e, t) + f_u(x_s + x_e, u_s + u_e, t) + g(x_s + x_e, t)w \tag{27}$$

With the proper feedback control model, the equation (27) can be simplified as:

$$\begin{aligned} dV &= f_1^*(V,\alpha)dt + g_1^*(V,\alpha)d\rho^* \\ d\alpha &= f_2^*(V,\alpha,q)dt + g_2^*(V,\alpha,q)d\rho^* \\ dq &= f_3^*(V,\alpha)dt + g_3^*(V,\alpha)d\rho^* \end{aligned} \tag{28}$$

with the observation equations:

$$\begin{aligned} P_t &= P_t[(1 - R(M_\infty))\cos^2(\alpha + \eta_i)R(M_\infty)] + P_{ni} \\ u_i &= V\cos(\theta_i + \alpha) + n_{ui} \\ u_j &= V\sin(\theta_j + \alpha) + n_{uj} \end{aligned} \tag{29}$$

Objective : Equations (28) and (29) form the complete filtering equations. In the Ito / Langevin Stochastic Differential Equation form:

$$\begin{aligned} dx &= f(x,t)\,dt + g(x,t)\,dw \\ dz &= h(x,t)dt + dn \end{aligned} \tag{30}$$

The filtering problem is to find the conditional mean of state variable x; and the filtering process requires knowledge of:

$$\begin{aligned} &\textit{A Posteriori} && p_x(x_t, t^*/Z) \text{ or } p_x^+(x_t, t) \\ &\textit{Conditional Density} && Z=\{z_t\} t \in [0, t^*] \\ &\textit{where} \end{aligned} \tag{31}$$

## VII. Visualization of conditional density propagation

The AHSV air data estimation problem involves soons to time-dependent nonlinear estimation equations [17]- [19]. Unfortunately, the solutions to these PDEs are infinite dimensional in nature. Exact solutions are rare (known for the linear dynamics case (Gaussian) and Bene's equation). In practice, some form of numerical approximation is unavoidable [18][20].

The Extended Kalman Filter is one of the approximations that is widely used because of its simplicity and because its moment equations are innovation independent. The EKF requires several assumptions on its conditional probability densities. Most importantly, the conditional probability density distributions must be symmetrical and unimodal such that the entire odd moments will vanish. Therefore it is desirable to analyze the time evolution of the conditional densities to validate the usage of EKFs.

An engineering method, which visualizes the characteristics of time dependent density functions without solving for the Zakai equation, would be highly desirable. The approach taken here is based on the numerical simulation. The AHSV dynamic model, in diffusion form, has been flown in the simulation for a large number of runs (10000 per flight condition) with the simulation setup shown in Fig. 19.

The collections of state error response ensembles are saved through multiple simulation runs. The collections of state error ensembles are then presented in a histogram format to represent the snapshots of state error probability. This result is also the graphical solution to the Fokker-Planck equation;

$$L(\cdot) = \sum_i \frac{\partial}{\partial x_i}(f_i(x_i, t)\cdot) + \frac{1}{2}\sum_{i,k}\frac{\partial}{\partial x_i \partial x_k}(g_i(x_i, t) g_k(x_i, t)\cdot) \tag{32}$$

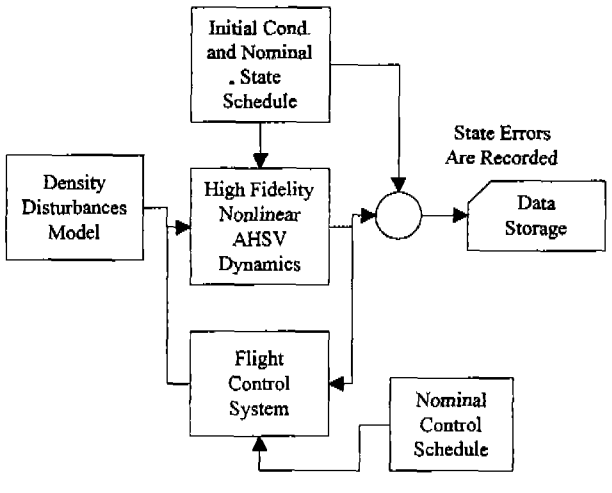


Fig. 19. Configuration of AHSV flight simulation.

Simulation results: The simulations were completed with 10000 runs per segment of the flight trajectory. The flight conditions corresponding to Mach numbers 10, 13, and 15 are selected. Each flight trajectory consisted of a 100 second flight segment. The 100 second duration was selected and considered adequate since most initial transients will die out within a few seconds into the flight as verified in the control system design section.

The size of fluctuations of the state variables about their nominal values will affect the apparent nonlinearities. It is suspected that as the magnitude of the fluctuation increases, the deformation of the densities will increase due to a larger nonlinearity effect. Therefore, the initial conditions and the driving disturbance noises (air-density fluctuations) were set to the maximum allowable values while keeping the flight conditions in a realistic range. The air-density disturbances were increased until the angle of attack response was approximately 0.5 degree r.m.s. at Mach 10, which is close to the maximum tolerable value for the stable operation of the controller.

The resulting histograms are shown in Fig. 20 to 23. As can easily be seen from the Figs, the densities retained the general shape of the Gaussian initial density. The results were consistent for all three segments of the nominal flight trajectories.

The air-density disturbances were further increased until significant distortion can be observed. The resulting histograms are shown in Figs 24 and 25. After about 5 seconds into the simulation run, the initial Gaussian density diffused and distorted into asymmetric probability distributions with multiple modes. At this time, the controller failed to stabilize the vehicle.

Within the narrow stable operating envelope, the observation process has been analyzed for the linearity through the nominal state trajectories. Because the nonlinearities involved in observation are mostly cosines and sines, and due to the small angular ranges of signals considered in this case, the observation process can be considered nearly linear, and the process will not deform the density significantly.

The evidences from the propagation of densities, and from the observation process suggest that if the initial condition satisfies Gaussian assumptions, then the propagation and update cycle will preserve the density shapes over time as long as the vehicle is in stable condition. These evidences suggest that the

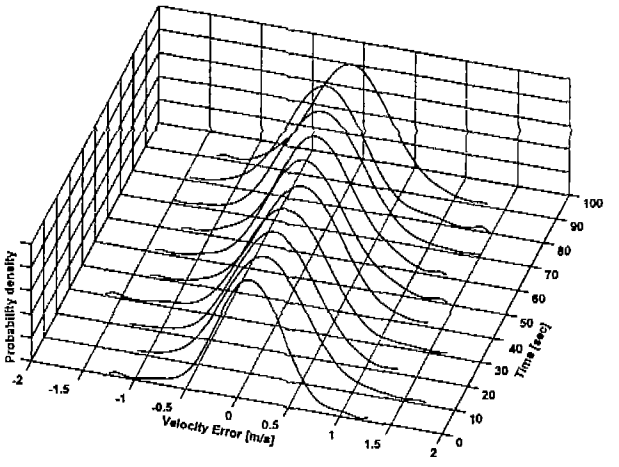


Fig. 20. Histogram of velocity error (mach 10 nominal operation).

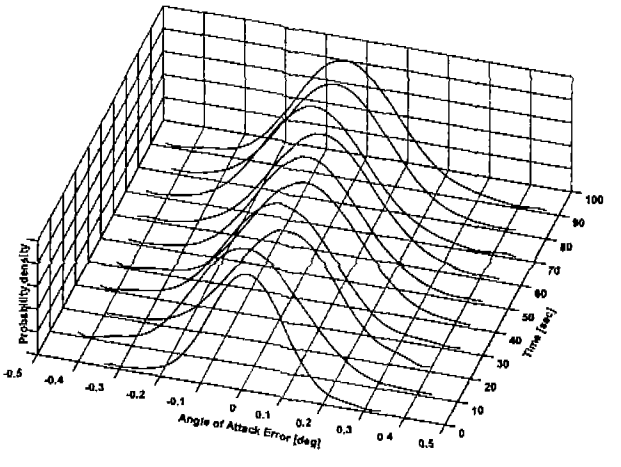


Fig. 21. Histogram of angle of attack error (mach 10 nominal operation).

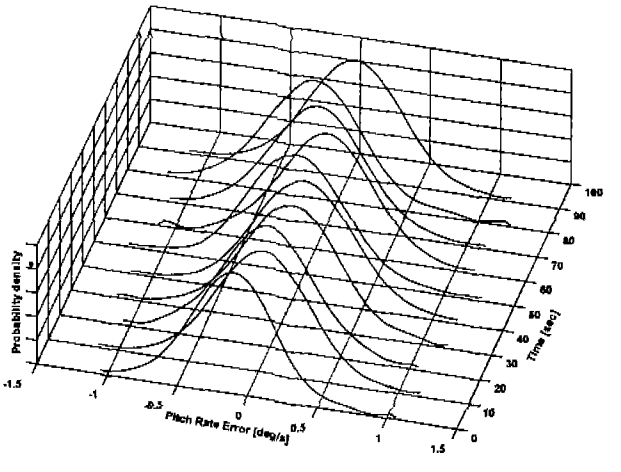


Fig. 22. Histogram of pitch rate error (mach 10 nominal operation).

Extended Kalman Filter should work satisfactorily for the considered range of the flight envelope.

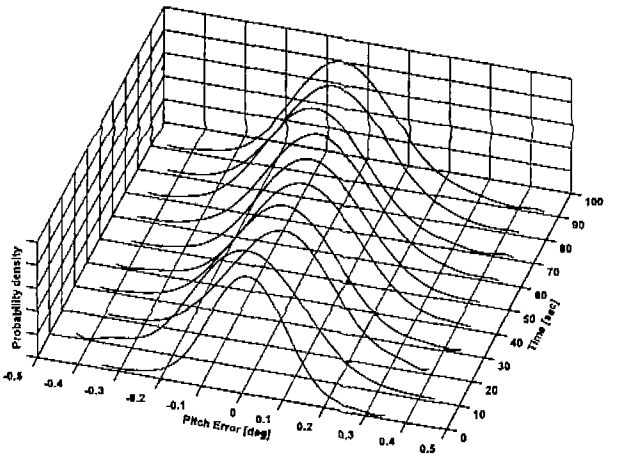


Fig. 23. Histogram of pitch error (mach 10 nominal operation).

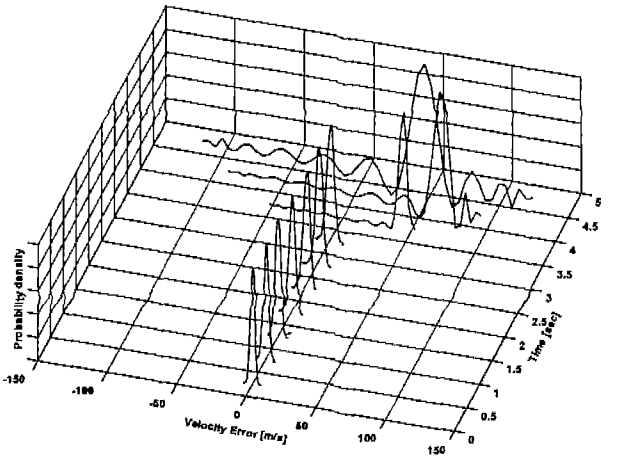


Fig. 24. Histogram of velocity error (mach 10 large disturbances - unstable).

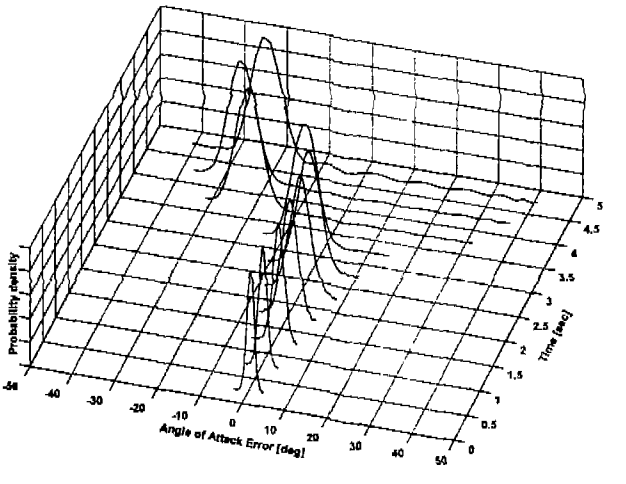


Fig. 25. Histogram of angle of attack error (mach 10 large disturbances - unstable).

## VIII. Extended kalman filter devel opment

The evidence shown by Visualization of Conditional Density Propagation suggested that the Extended Kalman Filter is applicable for the hypersonic flight

condition from Mach 10 to 15. A continuous - discrete form of EKF is implemented. The equations (28) and (29) can be stated simply as:

$$\dot{x}(t) = f(x, t) + g(x, t)w(t)$$
$$z(k) = h(x(k), k) + n(k) \tag{33}$$

where {w(t)} and {n(t)} are zero-mean, white Gaussian noise processes with:

$$\varepsilon\{w(t)w(\tau)^T\} = Q(t)\delta(t-\tau) \text{ and}$$
$$\varepsilon\{n(t)n(\tau)^T\} = R(t)\delta(t-\tau)$$

and for $t \geq t_0$ and $x(t_0) \equiv N(x_0, P_0)$ and $k=t_k$. The problem is specialized by assuming the case of uncorrelated process and sensor noise.

With the linearization defined as:

$$F(\hat{x}, t) \equiv \frac{\partial f(x, t)}{\partial x}\Big|_{x=\hat{x}} \text{ and } H(\hat{x}, t) \equiv \frac{\partial h(x, t)}{\partial x}\Big|_{x=\hat{x}} \tag{34}$$

the resulting EKF implementation is:

Propagation:

$$\dot{\hat{x}}(t) = m(\hat{x}(t), t)$$

$$\dot{P}(t) = F(\hat{x}(t), t)P(t) + P(t)F(\hat{x}(t), t)^T + SQ(t)S^T$$

Update:

$$\hat{x}(k+1/k+1) = \hat{x}(k+1/k) + K(k+1)[z(k+1) - h(\hat{x}(k+1/k))]$$

$$P(k+1/k+1) = [I - K(k+1)H(\hat{x}(k+1/k))]P(k+1/k)$$

$$K(k+1) = P(k+1/k)H(\hat{x}(k+1/k))^T * [$$

$$H(\hat{x}(k+1/k))P(k+1/k)H(x(k+1/k))^T + R(k+1)]^{-1}$$

(note: $\tilde{x}(t) = x(t) - \hat{x}(t)$ is the estimation residual or estimation error and $\hat{x}(k+1/k)$ is the estimate at time k+1 given measurements up to k)

Detailed linearization results and implementation issues are described in Reference 16.

Simulation results: The Monte Carlo simulation has been performed with the vehicle, sensors and estimator running simultaneously. The nominal flight conditions are the flight velocity of 3000m/s, 2.7 degree angle of attack (design value for steady state), and zero pitch rate. The external disturbances are chosen to match the effective acceleration disturbances, and they are: 0.1m/s$^2$ (roughly 1/100th of g) axial acceleration, 0.1 deg./sec. angle of attack rate, and 0.01deg./s$^2$ pitch acceleration. These flight conditions and the effective acceleration are considered to be a mild operating condition. The initial state covariance matrix was assumed to be uncorrelated and thus the diagonal form with the state uncertainties of 1 to 10 m/s in velocity error, 1 degree angle of attack error and 0.01 deg/sec pitch rate error.

The air-data sensor configuration consisted of a realistic Fig. based on available technology. The pressure sensor accuracy of 2% (SEADS) and the Rayleigh Scattering sensor with 0.8% accuracy were used for the simulation. Since the air data sensor noise characteristics can be known a priori with a relatively good accuracy, the filter noise covariance matrix was assumed to be the uncorrelated diagonal form with the 2% and 0.8% respectively from the nominal.

A set of typical estimator response is plotted in Figs 25 through 27. The angle of attack estimation error response is plotted in Fig. 28. As shown in Fig. 28,

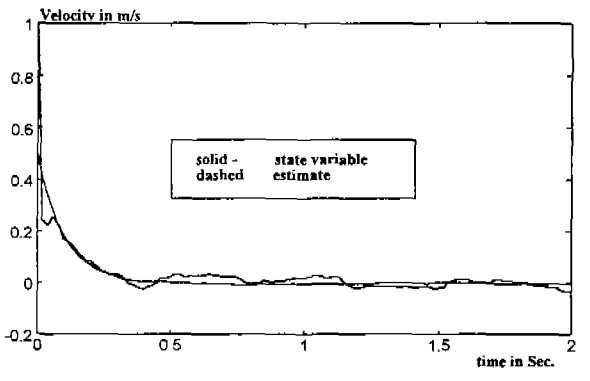


Fig. 26. True air velocity tracking error and estimate.

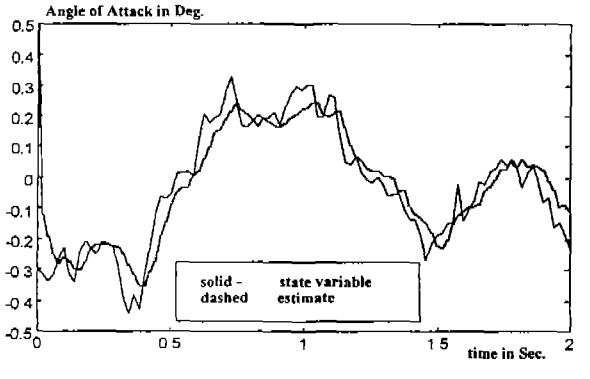


Fig. 27. Angle of attack perturbation trajectory and angle of attack estimate.

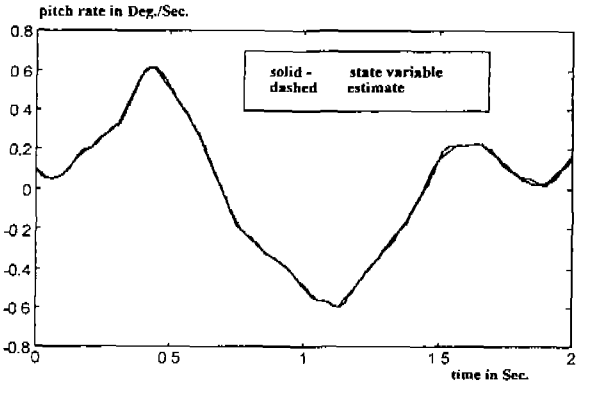


Fig. 28. Pitch rate trajectory and pitch rate estimate.

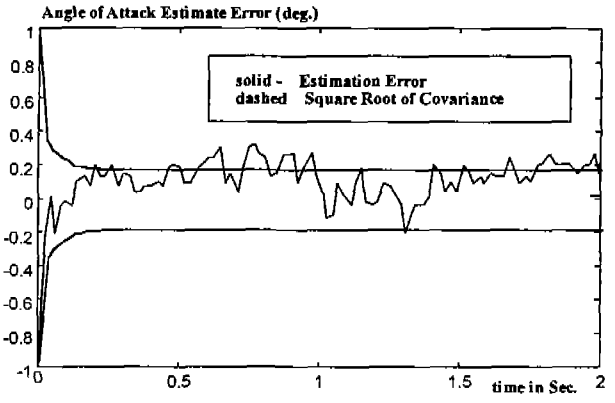


Fig. 29. Estimator performance (angle of attack estimation error).

the achieved performance was off by factor of 2 from the required accuracy of 0.1 degrees. Since the SEADS performance was about 0.5 degree in angle of attack, the improvements achieved by the EKF implementation are limited to a factor of two. These results suggest that the sensor hardware improvements are necessary for further accuracy gains, but less than order of magnitude improvements are needed.

## References

[1] R. J. Pegg, "National aero-space plane," *NASA Briefing to the Congressional Aeronautical Advisory Committee*, March, 1988.

[2] D. K. Schmidt, F. Chavez, "An integrated analytical aeropropulsive/aeroelastic model for the dynamic analysis of hypersonic vehicles," *AIAA paper 92-4567, Presented at the Atmospheric Flight Mechanics Conference*, August, 1992.

[3] D. K. Schmidt, J. Schierman, S. Garg, "Analysis of airframe/engine interactions - an integrated control perspective," *Proceedings of the Joint Propulsion Conference*, Paper no. 90-1918 (Also to appear in the Journal of Guidance, Control and dynamics)

[4] B. H.Kang, R. J. Hansman "Preliminary definition of pressure sensing requirements for hypersonic vehicles," *AIAA Paper 88-4652-CP*, September 7, 1988.

[5] P. D. Hattis, "Hypersonic vehicle air data collection : assessing the relationship between the sensor and guidance and control system requirements," *American Automatic Control Conference*, San Diego, CA. May, pp. 23-25, 1990.

[6] P. D. Hattis, "Propulsion and thermal inputs to HSV air data sensor design requirements," *CDSL Intralab Memorandum EGD-90-019*, February 1, 1990.

[7] P. D. Hattis, "A look at data integration studies and issues relevant to the hypersonic vehicle air data problem," *CDSL Intralab Memorandum EGD-89-087*, November 14, 1989.

[8] G. E. Chamitoff, "Robust intelligent flight control for hypersonic vehicles," *CSDL-T-1106, Draper Report, Also in MIT Ph.D. Thesis, Department of Aeronautics & Astronautics*, February, 1992.

[9] L. Webb, "Characteristic and use of X-15 air data sensors," *NASA TND-4597*, November, 1967.

[10] E. Hillje, "The orbiter air data system," *AIAA Paper*, 1983.

[11] P. D. Hattis, "A look at air data sensor candidates for hypersonic vehicles," *CDSL Intralab Memorandum ESC-92-052*, February 7, 1992.

[12] E. R. Hillje, D. E. Tymms, "Wind tunnel and flight calibration of the shuttle orbiter air data system," *AIAA Paper 78-792*, April 1978.

[13] R. B. Miles, D. A.Santavicca, M. Zimmermann, "Evaluation of non-intrusive flow measurement techniques for a re-entry flight experiment," *NASA Contractor Report 172142*, November, 1983.

[14] E. T. Benser, Honeywell Systems and Research Center (Minn.), "Proposed system functional requirements for a NASP type Vehicle Air Data System," *NASP Contractor Report 1044*, June, 1989.

[15] B. R. Tibbetts, W. R. Lempert, R. B. Miles, P. D. Jr. Kenefick, "Optically-based air-data system," *10th National Aero-Space Plane Technology Symposium, Paper # 185*, April, pp. 23-26, 1991.

[16] B. H. Kang, "Air-data estimation for air- breathing hypersonic vehicles," *CSDL-T -1257, Draper Report, Also in MIT Ph.D. Thesis, Dertnt of Aeronautics & Astronautics*, October, 1995.

[17] M. Zakai, "On the optimal filtering of diffusion processes," *Z. Wahr. Verw. Gebiete, 11*, pp. 230-243, 1969.

[18] R. H. Lamb, Jr. "Parametric nonlinear filtering," *LIDS-TH-1723, Lab. for Information and Decision Systems, thesis MIT, Department of Electrical Engineering & Computer Science*, May,1987.

[19] R. Brockett, "Nonlinear systems and nonlinear estimation theory," *NASA Technical Notes, N82-21986.*

[20] C. O. Culver, "Optimal estimation for nonlinear stochastic systems," *Ph.D. Thesis,instrumentation lab, MIT*, 1969.

**Bryan Heejin Kang**

B.S., Aerospace Engineering, University of Southern California, 1987. S.M., Aeroautics & Astronautics, MIT, 1989. Ph.D., Aeronautics & Astronautics, MIT, 1996. Senior Research Engineer, S &TD Avionics, TRW, 1996-Present Areas of interest include satellite attitude deterimination and control, nonlinear estimation, and hypersonic vehicle control.